

## **Subproject A2.5**

# **Structural and Chemical Properties of Quantum Dot Structures (D. Litvinov, D. Gerthsen)**

**Principle Investigator: Dimitri Litvinov, Dagmar Gerthsen**

**CFN-Financed Scientists: Dimitri Litvinov (1 BAT III, 48 months), Sabine Freidank Kalhöfer (1 BAT IVb, 24 months)**

**Further Scientists: Dr. habil. Reinhard Schneider, Holger Blank, Pascal Bockstaller (Diplom student), Roman Walther (Diplom student)**

**Laboratorium für Elektronenmikroskopie  
Karlsruhe Institut für Technologie**

## Structural and Chemical Properties of Quantum Dots

### Introduction and Summary

Heterostructures consisting of In(Ga)As quantum dots (QDs) embedded in GaAs are the basis of numerous (opto)electronic devices. They are also considered as promising candidates for quantum computation devices [1] using the spin of an electron stored in a QD as quantum bit. One reason for the large potential, that is attributed to InAs-QD-based quantum bits, are the long spin lifetimes [2] which are a prerequisite for the realization of spin devices.

Generally, QD formation in the InAs/GaAs system is the result of a growth-mode transition from two-dimensional (2D) layer-by-layer to three-dimensional (3D) island growth which is commonly referred to as Stranski-Krastanow growth mode. Due to the variety of In(Ga)As QDs with respect to size, chemical composition and shape, which can be fabricated depending on the growth technique and deposition conditions, the properties of In(Ga)As QD structures were systematically studied by transmission electron microscopy (TEM) in subproject A2.5. The work between 2006 and 2009 was focused on basic studies of molecular beam epitaxy (MBE) growth of InAs QDs, structural and chemical properties of InAs QDs, spin aligning layers and spin light emitting devices (spin LEDs). The following short summary lists the topics and the corresponding publications (see list of publications of the project), which were addressed in collaboration with the other groups in project A2 and projects A1.4 and A1.5.

- a) Correlation between all relevant MBE-growth parameters and QD properties [A2.5:9, A2.5:12, A2.5:15, A2.5:24].
- b) Identification of MBE conditions for obtaining large QDs with high In-concentration to reach luminescence at a wavelength of 1.3  $\mu\text{m}$  or longer which is important with respect to devices in telecommunication technology [A2.5:12, A2.5:15].
- c) Investigation of the In-segregation during the growth of InAs/GaAs heterostructures which is correlated with the 2D-3D growth-mode transition [A2.5:2, A2.5:4, A2.5:7, A2.5:11, A2.5:22, A2.5:24].
- d) Investigation of spin LEDs fabricated in projects A2.2 and A2.3, correlation of the structural properties of the QDs and ZnMnSe spin aligner with the spin-polarization degree [A2.5:1, A2.5:5, A2.5:6, A2.5:20].
- e) Study of the properties of spin aligning  $\text{Zn}_x\text{Mn}_{1-x}\text{Se}$  epitaxial layers with ( $0 \leq x \leq 1$ ) on GaAs and the optimization of their spin aligning properties [A2.5:3]

Due to the lack of space in this report, not all above-mentioned topics can be covered. Instead, we focus on the only partially published results which were obtained since 2009.

Since 2009, the A2 project has moved to the next stage where InAs QDs need to be positioned at well-defined locations [A2.5:26]. This can be accomplished by prestructuring GaAs substrates (project A2.6) to initiate QD formation at predefined positions to achieve in this way a significant dilution of InAs QDs which is necessary for the manipulation of spins in single QDs (projects A2.3 and A2.8). Moreover, GaAs-based photonic crystal slab nanocavities containing InAs QDs (projects A1.4 and A1.5) are attractive for low-threshold lasing and for semiconductor quantum optics, especially for a strong coupling between a single QD and a single cavity mode [A2.5:18, A2.5:21, A2.5:23, A2.5:25].

From a methodical point of view the accuracy of composition analyses of QDs by TEM was improved by taking into account their three-dimensional morphology and embedding in a GaAs matrix with respect to the finite TEM sample thickness [A2.5:15, A2.5:22]. An essential ingredient for the chemical analysis of QDs is the evaluation technique CELFA (composition evaluation of lattice fringe analyses images [3]) developed in our group which allows compositional analyses on an atomic scale on the basis of high-resolution TEM (HRTEM) images. First electron tomography results are presented in this report on the real three-dimensional shape of InAs islands.

Another focus of project A2 since 2009 was the MBE growth and evaluation of group-III nitride nanostructures as spin devices (project A2.7). This step is motivated by slow spin dephasing in group-III nitrides possibly even at room temperature [4] which is attractive for spin devices. Such spin devices consist of Cu-doped GaN as spin-aligner and InN QDs embedded in GaN or GaN QDs in AlN for spin storage. We will present results in this report which are concerned with the optimization of plasma-assisted (PA) MBE growth of epitaxial AlN and InN layers on Si(111) substrates.

### 1. Correlation between QD properties and MBE growth parameters [A2.5:9, A2.5:12, A2.5:15, A2.5:24]

It is meanwhile well known that InAs QDs do often not consist of binary InAs but ternary InGaAs with a composition that may vary continuously over the QD volume [5,6]. The distribution of Ga and In is strongly inhomogeneous and affects the shape of the confinement potential and the energy levels of localized electronic QD states. Segregation of group-III elements (in particular In-segregation during GaAs-cap layer deposition), In-desorption, interdiffusion and lateral group-III element redistribution during growth interruptions all contribute to the resulting QD composition. Apart from intermixing effects, the structural properties (size, shape) of the QDs depend strongly on the MBE growth parameters (deposited amount of InAs, substrate temperature, beam-equivalent-pressure ratio BEPR, growth rate, growth interruptions after InAs deposition, composition of the cap layer). This is illustrated by Figs. 1(a,b) where color-coded In-concentrations are derived by CELFA from HRTEM cross-section images. The two analyzed QD-structures were grown on GaAs(001) substrates under almost identical conditions [A2.5:9, A2.5:12]. Only the InAs deposition rate was lowered from 0.08 ML/s (ML: monolayer corresponding to the amount of In and As contained in one {200} plane) for the structure in Fig. 1(a) to 0.0056 ML/s in Fig. 1(b).

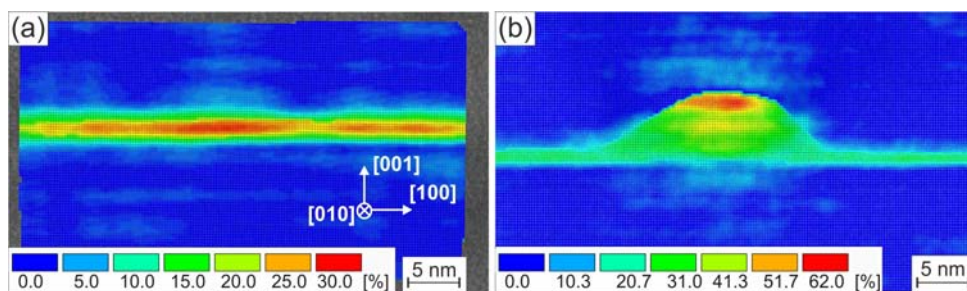


Fig. 1: Color-coded cross-section images of the In-distribution for QDs obtained with a deposition rate of (a) 0.08 ML/s and (b) 0.0056 ML/s under otherwise identical conditions (2.4 ML InAs, substrate temperature 500 °C, As<sub>4</sub>:In BEPR of 80:1 and a growth interruption of 10 s after the InAs deposition).

The In-distribution, In-concentration and structural properties differ significantly in these QD-structures. Essentially a layer with fluctuating In-concentration up to ~ 30 % with slightly varying

thickness around 6 nm is visible for the high-growth-rate sample (Fig. 1(a)). The regions with high In-concentration are assigned to the QDs which are embedded almost completely in the wetting layer (WL). Broadening of the WL occurs due to In-segregation during GaAs cap layer growth. According to Fig. 1(b), the QDs deposited with a low rate have the shape of a truncated pyramid with a height of approximately 12 nm, a width of about 45 nm at the bottom and about 20 nm at the top. In-concentrations up to 70 % are measured in the top part of the QD.

It has to be noted that the real In-concentrations inside the QDs are higher because we measure the In-concentration averaged over the TEM sample thickness. The measured In-concentration is lowered because the QDs are embedded in GaAs or in the wetting layer with a lower In-concentration. Although care must be exercised with respect to the interpretation of the evaluated compositions in Figs. 1(a,b) we find extremely high In-concentrations in QDs of the low-growth-rate sample which are not observed in all other samples. The efficient In-incorporation could be supported by the high BEPR which was found to reduce In-segregation during GaAs cap layer growth [A2.5:9]. The photoluminescence (PL) peak energy of low-growth-rate QD structures is only slightly above 1 eV, which corresponds to about 1.3  $\mu\text{m}$ , while the PL peak energy for the high-growth-rate sample is 1.18 eV. Further results on the influence of the MBE growth parameters can be found in [A2.5:9] where PL spectroscopy and TEM was applied to study the influence of all relevant MBE growth parameters.

Another strategy to shift the luminescence even further towards longer wavelengths is the overgrowth with  $\text{In}_x\text{Ga}_{1-x}\text{As}$  instead of binary GaAs [A2.5:15]. A series of samples was produced by MBE under identical growth conditions (substrate temperature 500  $^\circ\text{C}$ , 2.5 ML InAs at a low deposition rate of 0.006 ML/s). After a 10 s interruption, an  $\text{In}_x\text{Ga}_{1-x}\text{As}$  cap layer with In-concentrations  $x$  ( $x = 0, 0.05, 0.1, 0.15, 0.2, 0.25$ ) and a nominal thickness of 6 nm was grown and capped by 30 nm GaAs. The PL spectra of this sample series are presented in Fig. 2. Increasing the In-concentration in the cap layer from 0 % to 20 %, leads to a shift of the PL peak energy from 1.05 eV to 1.0 eV. The low PL intensity for the sample capped with  $\text{In}_{0.25}\text{Ga}_{0.75}\text{As}$  can be attributed to defect formation.

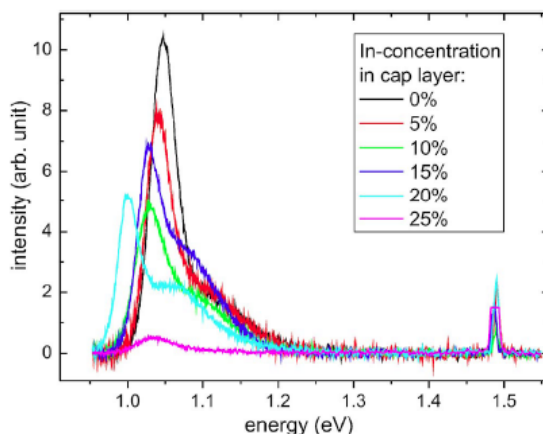


Fig. 2: PL spectra at 5 K of InGaAs QD samples with different In-concentration in the cap layer (concentrations given in the insert).

Fig. 3(a) shows the In-distribution of the QD structure with a  $\text{In}_{0.20}\text{Ga}_{0.80}\text{As}$  cap layer in a cross-sectional view with a measured maximum In-concentration around 50 %. A first approach to reconstruct the real In-concentration in the QDs is described in chapter 2 of this report which yields a maximum In-concentration of 90 % in the top part of this QD. It also shows that the In-concentration in the QDs does not depend significantly on the In-concentration of the cap layer (see

Fig. 7(b,d)). The main difference concerns the lateral QD-extension which increases from about 20 to 24 nm with increasing In-concentration in the cap layer (see Fig. 7(a,c)). In-concentration profiles along the growth direction through the WL and cap layer (as indicated by white frame in Fig. 3(a)) are plotted on Fig. 3(b).

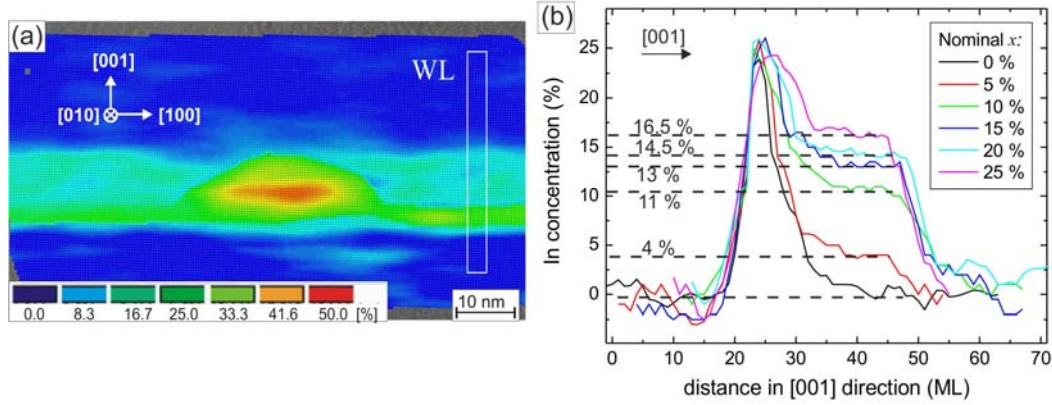


Fig. 3: (a) Color-coded map of the In-distribution of the InAs QD sample capped with 15 nm  $\text{In}_{0.20}\text{Ga}_{0.8}\text{As}$ . (b) Measured In-concentration profiles as a function of the distance in units of ML along the [001]-growth direction in the wetting-layer and cap region (as indicated by the white rectangle in Fig.3(a)).

The rise of the In-concentration at the InAs/GaAs-substrate interface is virtually identical in all samples but differences occur in the region of the  $\text{In}_x\text{Ga}_{1-x}\text{As}$  cap layers. For the GaAs-cap layer, the In-concentration profile is asymmetrical which can be attributed to segregation of accumulated indium on the WL surface during the GaAs-cap layer deposition. A segregation efficiency of 0.8 is derived on the basis of the model of Muraki et al. [7]. This value is characteristic for strong In-segregation because 80 % of the In-atoms segregate from the upper crystal layer into the newly deposited layer during growth. For samples capped with  $\text{In}_x\text{Ga}_{1-x}\text{As}$ , the In-concentration drops from the maximum to a plateau at lower In-concentration indicated by dashed lines in Fig. 3(b) with a width of 8–13 ML. These In-concentrations are consistently lower than the nominal In-concentrations – most likely due to lateral In-redistribution from the WL towards the QDs (with the exception of the sample capped with  $\text{In}_{0.1}\text{Ga}_{0.9}\text{As}$ , where the In-concentration in the cap layer was higher than the nominal one). The decrease of the In-concentration on the right-hand side of the profiles is determined by In-segregation during subsequent GaAs capping.

As outlined in [A2.5:15], the increasing In-concentration in the cap layer leads to a redshift of 47 meV of the PL peak associated with the ground state energies. This can be understood by the enlargement of the QDs and strain change due to the decrease of the mismatch between the QDs and cap layer.

Finally, we studied the influence of the substrate-temperature reduction during GaAs cap layer growth on the structural properties of InAs/GaAs QD structures [A2.5:24]. Three samples were fabricated with identical InAs QD layers but different temperatures  $T_{\text{cap}}$  (380 °C, 410 °C, 485 °C) during the deposition of the 50 nm GaAs cap layer.

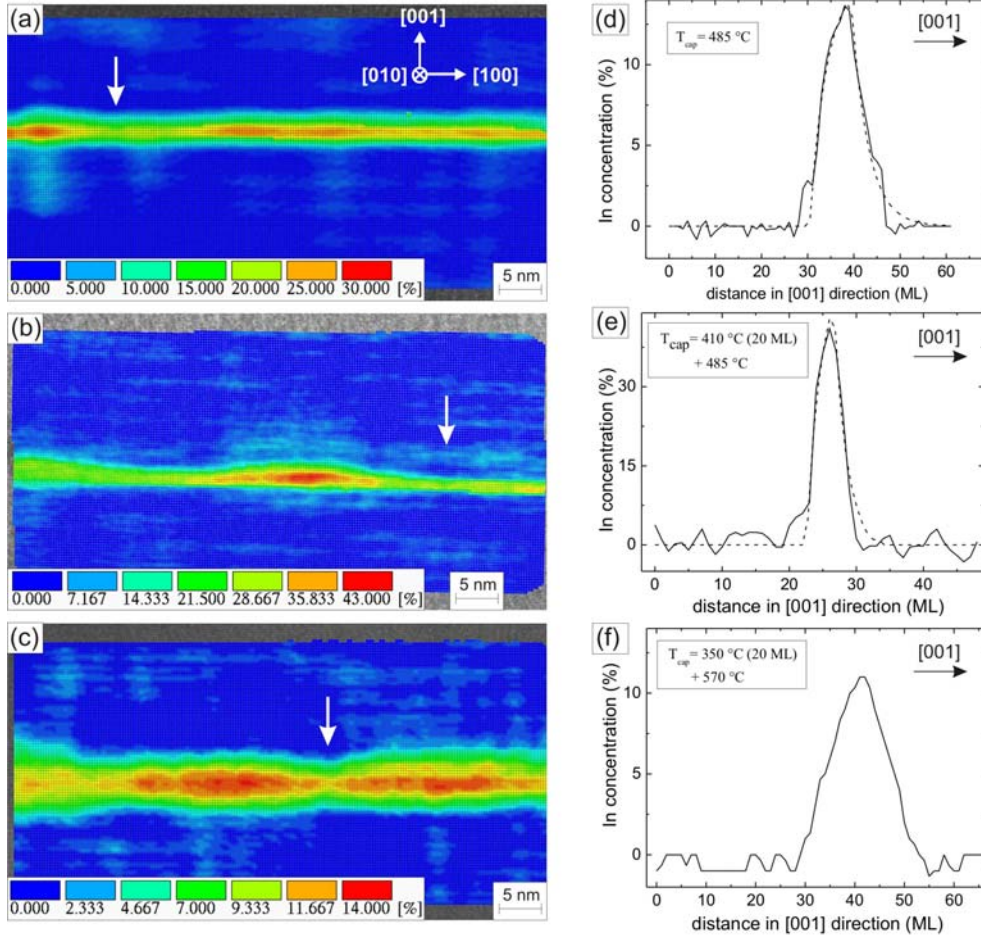


Figure 4: Color-coded cross-section maps of the In-distribution obtained by CELFA for samples (a)  $S_{485}$ , (b)  $S_{410}$  and (c)  $S_{350}$  and corresponding In-concentration profiles extracted from the WL regions marked by the arrows in the composition maps for samples (d)  $S_{485}$ , (e)  $S_{410}$  and (f)  $S_{350}$ .

According to Fig. 4, the reduction of  $T_{\text{cap}}$  has a strong effect on the In-distribution. Lowering  $T_{\text{cap}}$  from 485 °C to 410 °C leads to the decrease of the thickness of the WL with a full width at half maximum (FWHM) for sample  $S_{485}$  of 10 ML to 5 ML for  $S_{410}$ . The reduction of the WL width is compensated by an increase of In-concentrations with maximum values in the WL of 13 % in  $S_{485}$  and 27 % in  $S_{410}$  (Figs. 4(d,e)). These effects are a clear indication of the reduction of In-segregation. Sample  $S_{350}$  does not show the expected behavior (Figs. 4(c,f)) because a strong broadening of the In-distribution (WL with a FWHM of 13 ML) and a general reduction of the In-concentration is observed with an overall maximum In-concentration of only 14 %. We assume that interdiffusion occurred in this sample for the following reasons. A high concentration of point defects was probably introduced due to the low  $T_{\text{cap}}$  which is supported by the weak PL intensity of this sample. A potentially high vacancy concentration may lead to strong interdiffusion of In and Ga atoms after increasing  $T_{\text{cap}}$  from 380 °C after the deposition of 20 ML GaAs to 570 °C. The dominant influence of interdiffusion on the In-distribution is also supported by the symmetrical composition profile in Fig. 4(f) in contrast to the asymmetrical ones for  $S_{485}$  and  $S_{410}$ .

Segregation efficiencies  $R$  were determined on the basis of the measured profiles using Muraki model [7]. The fit curves (dashed lines) are included in Figs. 4(d,e). We obtain  $R = 0.76 \pm 0.02$  for

sample  $S_{485}$  and  $R = 0.59 \pm 0.09$  for sample  $S_{410}$ . The latter value has to be considered with caution because the temperature was changed during the growth. It was  $485\text{ }^\circ\text{C}$  for the ascending part of the profile during InAs deposition and  $410\text{ }^\circ\text{C}$  for the descending part associated with the cap-layer growth. It can be stated that lowering  $T_{\text{cap}}$  from  $485\text{ }^\circ\text{C}$  to  $410\text{ }^\circ\text{C}$  leads to an obvious reduction of segregation-induced intermixing which could indeed be utilized as a technique to maximize the indium content in QDs which are grown under optimized conditions for long-wavelength emission.

## 2. Reconstruction of the In-concentration in quantum dots [A2.5:15]

First steps towards the reconstruction of the real In-concentration of QDs embedded in GaAs were undertaken by the development of a suitable procedure and post-processing routine. The local TEM sample thickness and position of the QDs were determined by a tilt series with a  $[100]$ -tilt axis. At increasing tilt angles an apparent broadening of the dark WL region indicated by the arrows in Fig. 5(a-d) is observed. The QD with bright contrast in the dark WL is completely contained in the TEM sample, which is well visible in Fig. 5(b). Fig. 5(e) illustrates the principle which allows the determination of the TEM sample thickness  $t$  from the apparent broadening  $d$  of the WL contrast.

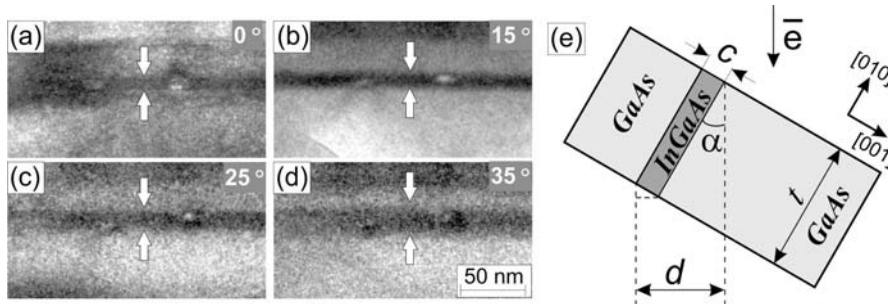


Fig. 5: Tilt series of (002) dark-field images of the same sample region at tilt angles of a)  $0^\circ$ , b)  $15^\circ$ , c)  $25^\circ$ , and d)  $35^\circ$ . e) Schematic illustration of the determination of the TEM specimen thickness.

The shape of the QDs was determined by HAADF (high-angle annular dark-field) scanning (S) TEM where the image intensity depends strongly on the local atomic number. An example is shown in Fig. 6(a) for a QD with a truncated pyramidal shape. The QD geometry is presented schematically in Fig. 6(b).

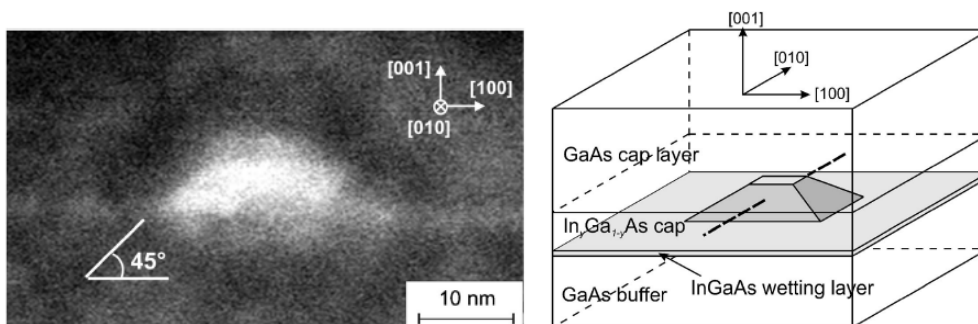


Fig. 6: (a) Cross-section HAADF STEM image of a QD with a truncated pyramidal shape. (b) Schematics of the geometry and shape of the QD morphology.

The knowledge of the TEM sample thickness, QD size and shape allows the reconstruction of the real In-concentration in the QD in a first approximation based on geometrical considerations. The results for QDs in the GaAs- and  $\text{In}_{0.2}\text{Ga}_{0.8}\text{As}$ -capped samples are presented in Fig. 7. The color-coded uncorrected In-distributions obtained from the CELFA evaluation are shown in Figs.

7(a,c). After post-processing of the data, In-concentrations of up to 90 % (note the different scales of the color coding in Fig. 7(b,d)) are obtained in the upper part of the QDs in both cases. Since the correction was only applied to the QD region, the WL is not visible in the corrected maps. We do not find significant differences for the In-concentration of the QDs in samples with a GaAs (Fig. 7(a,b)) or  $\text{In}_{0.2}\text{Ga}_{0.8}\text{As}$  cap layer (Fig. 7(c,d)). The white triangles indicate the QD shape and size. Obviously, the lateral size of the QDs increases with the In-concentration in the cap layer from about 20 nm for the sample with  $x = 0$  to 24 nm for the island with  $x = 0.2$ , while the QD height increases only slightly from 6.8 to 7.3 nm. The white arrows mark the maximum of the In-concentration within the dots which shifts upwards after the correction. In the cases of Fig. 7, (200) lattice-fringe images were taken (fringes oriented perpendicular to the substrate/layer-interface), which are less affected by inhomogeneous strain as the (002) lattice planes. The latter are oriented parallel to the interface and their distance and orientation changes within a QD which increases significantly the error of the composition determination.

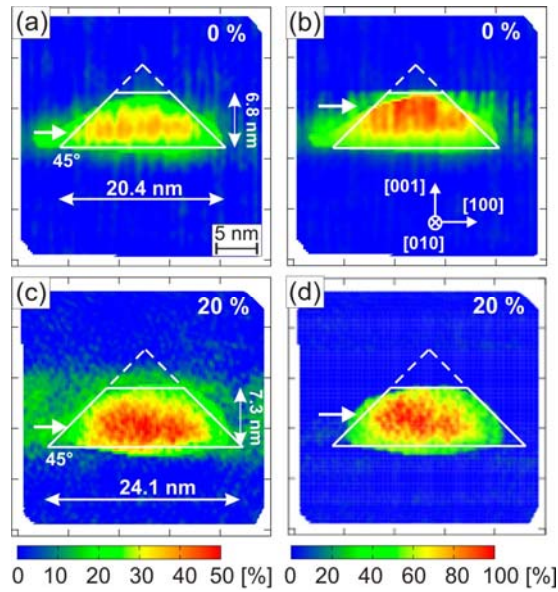


Fig. 7: Color-coded In-concentration maps obtained with CELFA in samples capped with (a,b) GaAs and (c,d)  $\text{In}_{0.2}\text{Ga}_{0.8}\text{As}$  before (left-hand side) and after post-processing of the CELFA data (right-hand side). The white triangles delineate the QD shape.

### 3. Electron tomography of InAs QDs

Recently electron tomography was applied as an alternative method to reconstruct the three-dimensional QD shape [8]. The reconstruction is based on tilt series of images within a tilt range of  $-70^\circ$  to  $70^\circ$  and an angular step interval of  $1^\circ$  using a single-tilt tomography holder in the FEI Titan<sup>3</sup> 80-300 microscope. The high-angle annular dark-field (HAADF) scanning (S) TEM mode is used for image acquisition because it provides strong chemical contrast (Z-contrast) [9]. It is also less sensitive towards contrast changes due to varying diffraction conditions because electrons scattered in large angles are collected for image formation.

Fig. 8(a) shows a cross-section HAADF STEM image of two uncapped InAs QDs on a GaAs(001) layer taken close to [010]-zone axis. The increased brightness of the QD on the left-hand side with respect to the GaAs visualizes the Z-contrast.

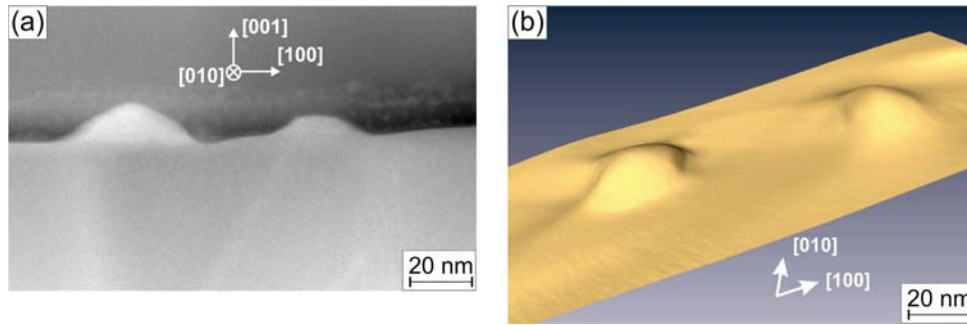


Fig. 8: (a) Cross-section HAADF STEM image of QDs taken close to the  $[010]$ -zone axis. (b) Reconstructed 3D shape of the QDs from a tilt series of HAADF STEM images taken in the angular range from  $-70^\circ$  to  $70^\circ$ .

The InAs island on the right-hand side appears darker because the local TEM-sample thickness is smaller in this case. Fig. 8(b) shows a 3D contour model which was reconstructed on the basis of 141 HAADF STEM images using a direct (unweighted) back projection [10-12] contained in the “FEI Inspect 3D” software package. Unweighted back projection usually results in a blurry low-quality image. However, in this case it simplifies the selection of the QD contour because a simple threshold filter was used to extract the contour.

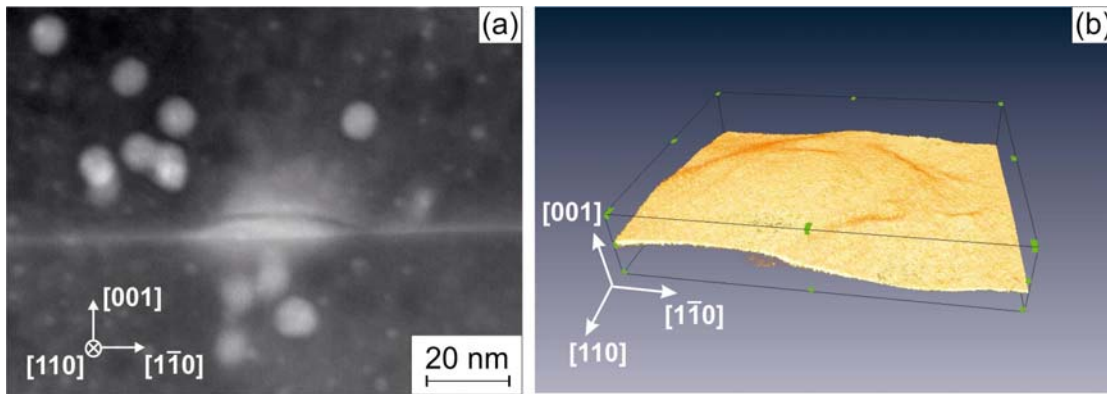


Fig. 9: (a) Cross-section HAADF STEM image of an InAs QD embedded in GaAs taken close to the  $[110]$ -zone axis. Gold markers of 10 nm size show bright contrast. (b) Reconstructed 3D image of the QD from a tilt series of HAADF STEM images taken in an angular range from  $-70^\circ$  to  $70^\circ$ .

Fig. 9(a) shows a cross-section HAADF STEM image of an InAs QD embedded in GaAs. We used gold nanoparticles with 10 nm diameter as alignment markers for the reconstruction procedure which show bright contrast in Fig. 9(a). The Au nanoparticles are deposited on the surface of the TEM cross-section sample. Applying a similar reconstruction procedure as for uncapped islands, we obtain a reconstructed 3D image of the embedded QDs (Fig. 9(b)). In the reconstructed images (Figs. 8(b) and 9(b)), facets along  $\langle 100 \rangle$  directions can be observed which correlates with our finding in [A2.5:15], where  $\{101\}$  facets of InAs QDs were observed.

#### 4. Growth of InAs QDs on prestructured GaAs(001) substrates [A2.5:26]

Electron-beam lithography (EBL) and suitable etching techniques were applied to prestructure holes in MBE-grown GaAs buffer layers with the aim to initiate InAs QD nucleation in these holes. The essential steps of the procedure comprise the removal of the resist, cleaning of the sample surface outside of the chamber and heating in the MBE chamber to remove residual organic contamination

in order to minimize defects and uncontrolled QD nucleation. A 16 nm GaAs buffer layer was then grown at 500 °C followed by 1.7ML of InAs. Details of the prestructuring and QD fabrication are described in [A2.5:26]. TEM was used to determine of the origin defects in the prestructured regions, which leads to a reduced photoluminescence intensity compared to InAs QD structures without prestructuring.

Fig. 10(a) shows an atomic force microscopy (AFM) image of an InAs QDs without GaAs cap layer. The islands are characterized by a height of 14 nm and different lateral sizes. The sample shows predominant double-dot nucleation per site. Fig. 10(b) shows cross-section HAADF STEM images (top) of the same sample with enlarged views (bottom) of prestructured areas (PAs). Focused-ion-beam (FIB) preparation is indispensable to obtain cross-section TEM samples with the PAs in the electron-transparent region of the TEM sample. According to the AFM image, there is predominant double-dot formation. In Fig. 10(b) we observe two islands of triangular shape in each PA marked by the black arrows.

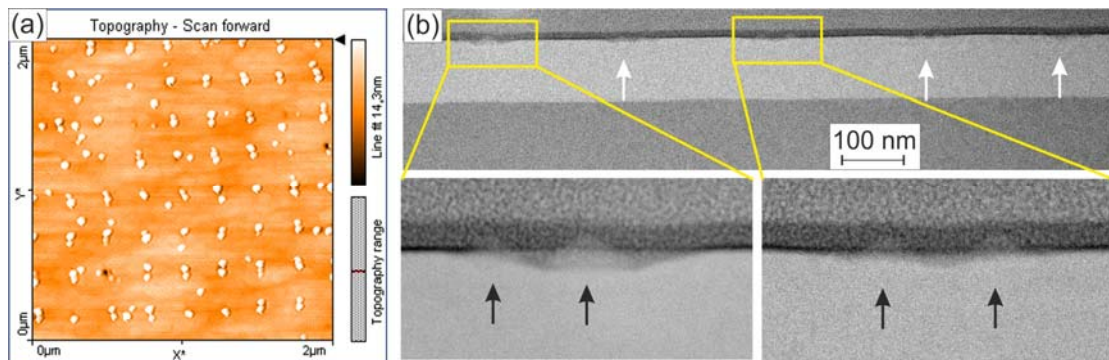


Fig. 10: (a) Atomic force microscopy image of surface. White points are InAs QDs, black points are holes. (b) Top: cross-section HAADF STEM image close to [110]-zone axis of sample with PAs (PAs - white arrows). Bottom: two enlarged views of PAs with two InAs QDs (black arrows).

Fig. 10(a) shows holes with dark contrast which is not defined by EBL and thus interferes with the attempt of deterministic QD positioning. The holes are less than 16 nm deep (in contrast to 30 nm for EBL-structured holes), which corresponds to the thickness of the GaAs buffer. This indicates that the defect holes originate from the regrowth interface.

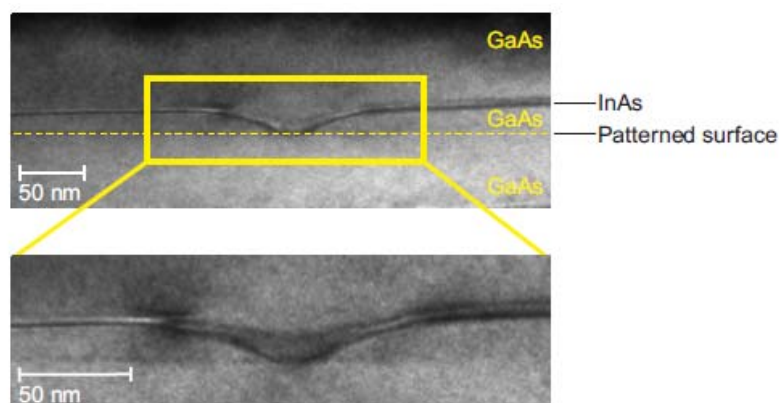


Fig. 11: Cross-section (002) dark-field TEM image (top) with enlarged view (bottom) of a defect hole originating from the regrowth interface.

Further confirmation is given by TEM analysis of a capped sample. Fig. 11 shows a cross-section TEM image of a defect hole in a prestructured sample. The different layers of the structure are visible. The patterned GaAs surface is indicated by a dashed line. The defect hole develops from the patterned surface upwards in the GaAs buffer layer. A local change on the patterned surface appears to inhibit the proper GaAs regrowth after EBL. InAs, however, then nucleates inside the hole, which is finally covered by the GaAs cap layer. The GaAs side walls of the defect hole exhibit a curved shape which implies that strain is accumulated at the surface of the GaAs buffer layer facing the site where nucleation of GaAs is impeded. Two factors can account for the occurrence of the described defect holes. First, incomplete removal of the native oxide could leave residual oxide compounds on the surface. Second, insufficient surface cleaning after the lithography process could cause local organic contamination of the sample. Both effects can affect proper regrowth after EBL.

## 5. Group-III-nitride heterostructures on Si(111)

Group-III nitrides are a new focus of the A2 project in the present funding period. Using group-III nitride nanostructures as spin devices is motivated by slow spin dephasing possibly even at room temperature [4]. The growth is carried out by plasma-assisted (PA) MBE in the group of D. Schaadt (project A2.7). The task of project A2.5 was the analysis of the structural quality of the group-III nitride layers in the process of growth optimization.

The growth of group-III nitrides (GaN, AlN InN and their ternary alloys) was carried out on Si(111) substrates which is a low-cost alternative compared to growth on other substrates such as sapphire or SiC. Silicon is also attractive due to its high thermal conductivity and the potential for integration with Si-based devices. The epitaxial growth of InN and GaN on silicon is difficult due to the presence of an amorphous layer at the interface [13] which induces 3D growth and the formation of polycrystalline material. However, the deposition of an AlN buffer layer greatly improves the quality of epitaxial GaN or InN epilayers [14-16] which was first optimized.

### 5.1. Optimization of AlN buffer layer growth on Si(111)

AlN layers with approximately 500 nm thicknesses were grown at temperatures between 600 °C and 900 °C under metal-rich conditions. These samples were studied by scanning electron microscopy (SEM) and TEM to determine the optimum substrate temperature  $T_{\text{sub}}$  for AlN growth. Four samples were grown under the same conditions apart from  $T_{\text{sub}}$  which was chosen to be 600 °C (sample  $S_{600}$ ), 700 °C (sample  $S_{700}$ ), 800 °C (sample  $S_{800}$ ) and 900 °C (sample  $S_{900}$ ). The fifth sample  $S_{900\text{Al}}$  was also grown at  $T_{\text{sub}} = 900$  °C but with a higher Al flux than sample  $S_{900}$ .

In Fig. 12 presents SEM images of the surface morphology of all samples on a large and small (inserts) scale. Large holes are observed on the surface of sample  $S_{600}$  (arrows in Fig. 12(a)). Large Al-drops occur on the surfaces of samples  $S_{700}$  (Fig. 12(b)) and  $S_{800}$  (Fig. 12(c)) as determined by energy-dispersive X-ray spectroscopy (EDXS). The number and size of the drops decrease with  $T_{\text{sub}}$ . Al-drops are not observed on the surface of  $S_{900}$  and  $S_{900\text{Al}}$ .

The inserts in Figs. 12(a-e) show structural details of the AlN surfaces. The surface of  $S_{600}$  consists of separate small structures (or columns) with six-fold symmetry (insert in Fig. 12(a)). Hexagonal island-like structures are observed on the surfaces of  $S_{700}$  and  $S_{800}$  (inserts in Figs. 12(b) and 12(c)). Their sizes increase with the substrate temperature. The surfaces of the samples grown at 900 °C contain small holes which marked by arrows. The number of holes decreases if the Al flux is increased (compare Fig. 12 (d) for  $S_{900}$  and Fig. 12(e) for  $S_{900\text{Al}}$ ). According to the SEM images,  $S_{900\text{Al}}$  provides the smoothest surface which is characterized with minimal defect density.

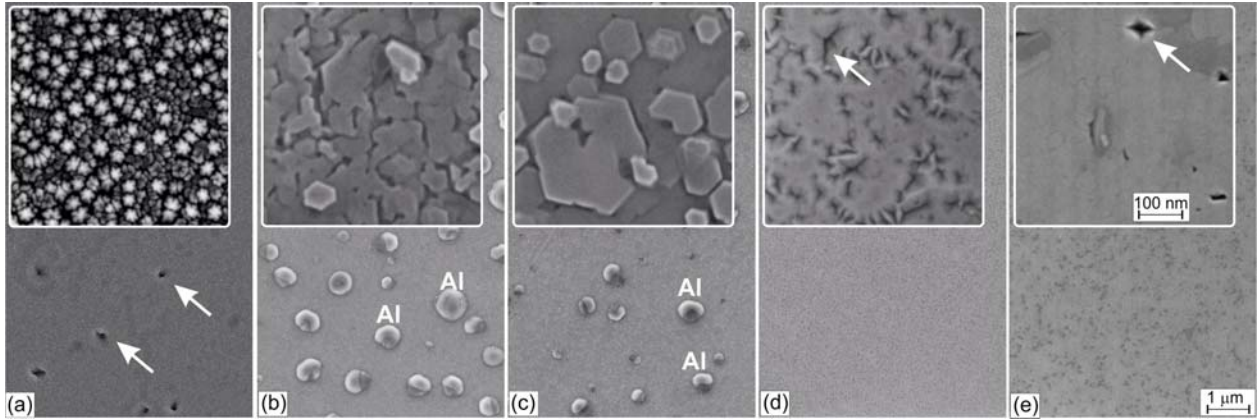


Fig. 12: (a-e) SEM images of the AlN surface of samples  $S_{600}$ ,  $S_{700}$ ,  $S_{800}$ ,  $S_{900}$  and  $S_{900Al}$  accordingly.

Fig 13(a) presents a  $(002)_{Si}$  dark-field cross-section TEM image of sample  $S_{900Al}$ . The density of threading dislocations in the AlN layer (marked by D) is significantly lower compared to the other investigated samples (images are not shown here). Two AlN regions can be distinguished in the HRTEM image Fig. 13(b). The area close to Si-substrate is about 30 nm thick and consists of AlN in the stable wurtzite (w). The region above contains the metastable cubic sphalerite (s) phase which is demonstrated by the Fourier transforms of the respective image sections (inserts in Fig. 13(b)). Both phases contain numerous stacking faults marked by  $SF_s$  and  $SF_w$ , which are oriented parallel and inclined to the AlN/Si interface.

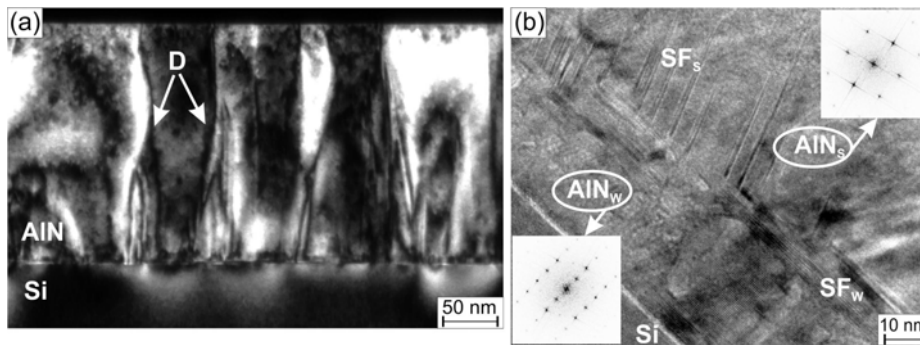


Fig. 13: (a)  $(002)_{Si}$  dark-field cross-section TEM image close to the  $[110]_{Si}$ -zone axis of sample  $S_{900Al}$ , containing dislocations (D) and (b) HRTEM cross-section TEM image close to  $[110]_{Si}$ -zone axis with FFT from two AlN regions of sample grown at  $900^{\circ}C$  with high Al flux. w – wurtzite phase, s – sphalerite phase, SF - stacking faults.

The interface region between AlN epilayer and Si-substrate of sample  $S_{800}$  contains regions with an elongated trapezoidal shape which extend from the interface into the Si-substrate as illustrated by the HAADF STEM cross-section image Fig. 14. EDXS mappings of the Si, Al and N distributions (right-hand side of Fig. 14) in the area marked by the white square in Fig. 14(a) show that this region consists of pure Al.

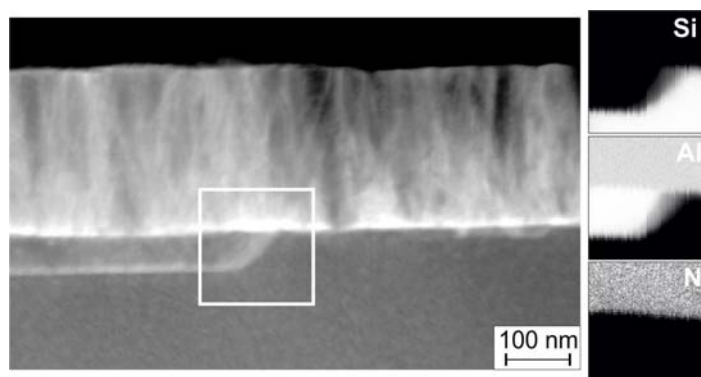


Fig. 14: (left) HAADF STEM image close to the  $[110]_{\text{Si}}$ -zone axis of sample grown at  $800^{\circ}\text{C}$  and (right) EDXS maps of elements Si, Al and N from area limited by white quadrate.

Diffraction patterns of the Al-region (not presented here) demonstrate that the Al is epitaxially oriented with respect to the Si-substrate. An Al layer between Si(111) substrate and AlN layer was also observed by Kaiser et al. [17] after AlN deposition between  $800^{\circ}\text{C}$  and  $900^{\circ}\text{C}$  under Al-rich conditions. They explained this phenomenon by the existence of a low-temperature eutectic transformation which takes place in the SiAl system below  $577^{\circ}\text{C}$ . If excess Al is present on the substrate surface this may lead to the dissolution of Si in Al because a liquid solution is formed above the eutectic temperature of  $577^{\circ}\text{C}$  in the AlSi binary system [18]. This scenario is expected for sample  $S_{800}$  which was grown under high Al-rich conditions as visualized by the Al drops on the AlN surface (Fig. 12(c)). We do not observe Al-inclusions in the samples grown at  $900^{\circ}\text{C}$  despite Al-rich growth conditions which is explained by the high Al-desorption rate. This interpretation is supported by the lack of Al-droplets on the surface (see Figs. 12(d,e)).

According to TEM and SEM, the AlN layer with the best quality (lowest dislocation density, smooth surface) is obtained for the sample grown at  $900^{\circ}\text{C}$  under Al-rich conditions. This is substantiated by the full-width at half-maximum of the AlN(0002) reflection obtained by high-resolution X-ray diffractometry which decreases from  $5898.5$  arcsec for films grown at  $600^{\circ}\text{C}$  to  $1784.9$  arcsec for films grown at  $900^{\circ}\text{C}$ .

## 5.2. Cu-doped GaN on AlN/Si(111)

For the injection of spin-polarized charge carriers into QDs, a ferromagnetic spin-aligning layer is required which yields a high spin-polarization degree ideally even at room-temperature. The most promising candidates for such a ferromagnetic layer are diluted magnetic semiconductors (DMS), which may exhibit ferromagnetism if a small percentage of group-III elements are replaced by transition metals. However, magnetic dopants like manganese may lead to confusing results, because magnetic clusters in an otherwise nonmagnetic layer may occur which are not suited for spin alignment of charge carriers. The non-magnetic dopant copper is a promising candidate in GaN as well because theoretical predictions show a maximal spin-polarization of 100% and a high Curie-temperature above  $350\text{ K}$  [19]. A few experimental studies have indicated indeed ferromagnetism in Cu-doped nitrides.

Fig 15(a) shows a cross-section bright-field TEM image of a sample with a  $100\text{ nm}$  thick Cu-doped GaN layer grown at  $700^{\circ}\text{C}$  on AlN( $100\text{ nm}$ )/Si(111). The energy-filtered TEM image (Cu- $L_{2,3}$  edge) in Fig. 15(b) shows the Cu-distribution in the GaN layer. Cu-rich regions (marked by arrows)

in the GaN layer can be seen close to the GaN/AlN interface. EDXS measurements in the Cu-doped GaN layer (Fig. 15(c)) yields an average Cu-concentration of about 1.2%.

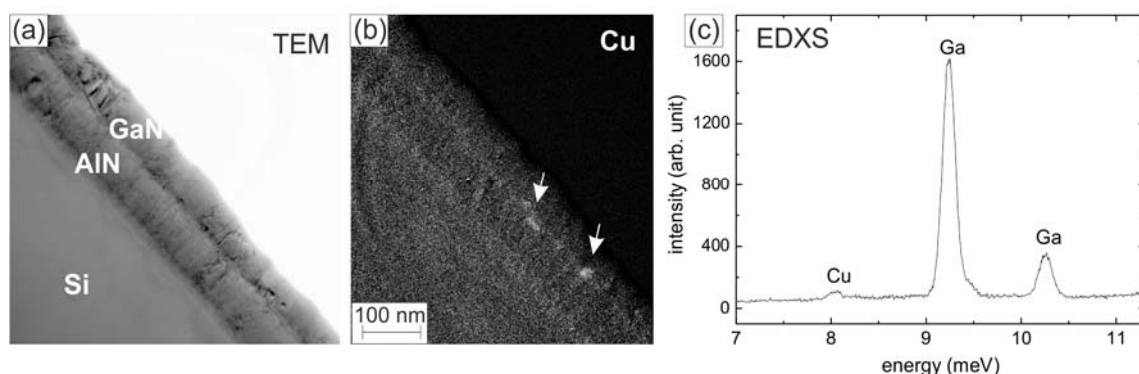


Fig. 15: (a) Bright-field cross-section TEM image of a sample grown at 700°C with a Cu-doped GaN layer and (b) Cu-map obtained with energy-filtered TEM (Cu-L<sub>2,3</sub> edge). (c) EDX spectrum obtained in Cu-doped GaN layer.

Further optimization of the growth of Cu-doped GaN is in progress to achieve reproducible ferromagnetic behavior.

### 5.3 InN layers on AlN/Si(111)

InN layers with approximately 500 nm thicknesses were grown on AlN/Si(111) under metal-rich conditions. The AlN buffer of 30 nm thickness was grown at  $T_{\text{sub}} = 880$  °C prior to InN deposition. Three samples were investigated with InN growth temperatures of 325 °C (sample S<sub>325</sub>), 350 °C (sample S<sub>350</sub>) and 375 °C (sample S<sub>375</sub>) under otherwise identical conditions.

Figs. 16 shows bright-field TEM cross-section images of samples S<sub>325</sub> (Fig. 16(a)) and at S<sub>350</sub> (Fig.16(b)). The InN layers contain threading dislocations and inversion domains. We note that the dislocation density is significantly smaller than in an AlN layer with comparable thickness (Fig. 13(a)).

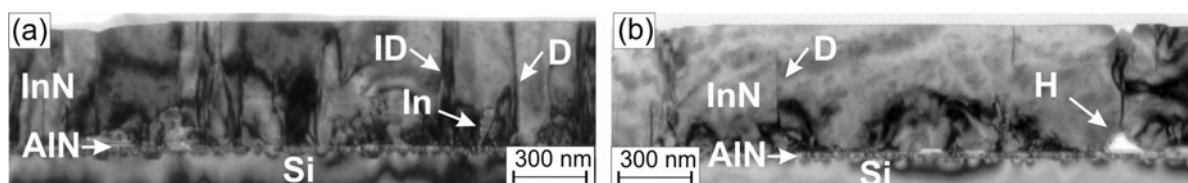


Fig. 16: Bright-field cross-section TEM images of samples S<sub>325</sub> (a) and S<sub>350</sub> (b). “D” mark dislocations, “ID” inversion domains, “In” In-inclusions and “H” holes.

Holes (H in Fig. 16(b)) are observed close to the InN/AlN interface in samples grown at higher temperatures. Moreover, regions containing pure indium und indiumoxide are embedded in the InN layers. The latter material is responsible for a high-energy photoluminescence signal at 1.89 eV which was confused with the InN luminescence in earlier work, but more recently several groups reported about an InN band-gap energy between 0.65 and 0.90 eV [13]. Based on the TEM analyses we conclude that the optimum growth temperature for InN is 325 °C which yields layers without holes and a smooth surface.

## References

- own work with complete titles -

- [1] M. Bayer, P. Hawrylak, K. Hinzer, S. Fafard, M. Korkusinki, Z.R. Wasilewski, O. Stern, A. Forchel, *Science* **291**, 451 (2008)
- [2] E. Tsitsishvili, R. v. Baltz, H. Kalt, *Phys. Rev. B* **67**, 205330 (2005)
- [3] A. Rosenauer, D. Gerthsen, *Advances in Imaging and Electron Physics* **107**, 121 (1999), and A. Rosenauer, *Transmission Electron Microscopy of Semiconductor Nanostructures - An Analysis of Composition and Strain* (Heidelberg, Springer), Springer Tracts in Modern Physics, **182** (2003).
- [4] S. Krishnamurthy, M. van Schilfgarde, N. Newman, *Appl. Phys. Lett.* **83**, 1761 (2003)
- [5] B. Lita, R. S. Goldman, J. D. Phillips, P. K. Bhattacharya, *Appl. Phys. Lett.* **75**, 2792 (1999)
- [6] A. Rosenauer, D. Gerthsen, D. Van Dyck, M. Arzberger, G. Böhm, G. Abstreiter, *Quantification of segregation and mass transport in  $In_xGa_{1-x}As/GaAs$  Stranski-Krastanow layers*, *Phys. Rev. B* **64**, 245334 (2001)
- [7] K. Muraki, S. Fukatsu, Y. Shiraki, R. Ito, *Appl. Phys. Lett.* **61**, 557 (1992)
- [8] R. Beanland, A. M. Sanchez, J. C. Hernandez-Garrido, D. Wolf, and P. A. Midgley, *J. Microscopy* **237**, 148 (2009)
- [9] L. Reimer: *Scanning Electron Microscopy: Physics of Image Formation and Microanalysis* (Springer, Berlin 1998).
- [10] W. Hoppe, R. Langer, G. Knesch, C. Poppe, *Naturwissenschaften* **55**, 333 (1968)
- [11] R. A. Crowther, D. J. de Rosier, A. Klug, *Proc. R. Soc. London A* **317**, 319 (1970)
- [12] G. T. Herman, *Image Reconstruction from Projections. In: The Fundamentals of Computerised Tomography* (Academic Press, New York, 1980)
- [13] A. G. Bhuiyan, A. Hashimoto, and A. Yamamoto, *J. Appl. Phys.* **94**, 27793 (2003) and references therein
- [14] H. Lahreche, P. Vennegues, O. Tottereau, M. Laügt, P. Lorenzini, M. Leroux, B. Beaumont, P. Gibart, *J. Cryst. Growth* **217**, 13 (2000)
- [15] M. D. Kim, S. R. Park, J. E. Oh, S. G. Kim, W. C. Yang, Bun-Hei Koo, *J. Cryst. Growth* **311**, 2016 (2009)
- [16] C.-L. Wu, C.-H. Shen, H.-Y. Chen, S.-J. Tsai, H.-W. Lin, H.-M. Lee, S. Gwo, T.-F., Chuang, H.-S. Chang, T.M. Hsu, *J. Cryst. Growth* **288**, 247 (2006)
- [17] U. Kaiser, I. I. Khodos, J. Jinschek, and W. Richter, *J. Electron Micr.* **48**, 545 (1999)
- [18] M. Hansen and K. Anderko, *in: Solution of binary alloys* (McGraw-Hill, New York, 1958), p. 133
- [19] R. Q. Wu, G. W. Peng, L. Liu, Y. P. Feng, Z. G. Huang, and Q. Y. Wu, *Appl. Phys. Lett.* **89**, 062505 (2006)